Chapter 5

Ice Filling Experiments

5.1 Chapter Summary

These experiments demonstrate for the first time the deposition of subsurface ice directly from atmospheric water vapor under Mars surface conditions. Deposition occurs at pressures below the triple point of water, and therefore in the absence of a bulk liquid phase. Significant quantities of ice are observed to deposit in porous medium interstices; the maximum filling fraction observed in the experiments is ~90%, but the evidence is consistent with ice density in pore spaces asymptotically approaching 100% filling. The micromorphology of the deposited ice reveals several noteworthy characteristics including preferential early deposition at grain contact points, complete pore filling between some grains, and captured atmospheric gas bubbles. The boundary between ice-bearing and ice-free soil, the "ice table", is a sharp interface, consistent with theoretical investigations of subsurface ice dynamics. Changes of surface albedo are shown to affect ice table morphology through their modulation of the local temperature profile. A variety of atmospheric humidity regimes and experiment durations are employed to provide information about the rate at which the pores fill. Accumulation of ice is shown to reduce the diffusive flux and thus hinder further ice deposition via constriction of available pore space. Numerical models of the experiments based on diffusion physics are able to reproduce experimental ice contents if the constriction parameterization has expected contributions in addition to reduced porosity. Several phenomena related to the evolution of subsurface ice are discussed in light of these results and interpretations are given for a range of potential observations to be made by the Phoenix Scout Lander.

5.2 Parameter Choices

The atmosphere of present-day Mars is dry, and the upper levels of the regolith are subject to ice-filling vapor density gradients on the order of 10^{-6} kg m^{-4}. Under these conditions, the maximum rate of ice deposition would fill a regolith with ~40% porosity in approximately 10^5 years. Obviously,

such timescales are impractical for measurable ice contents to be developed in the laboratory. To enhance the deposition rate, a more humid atmosphere and a stronger vapor density gradient than found on Mars today are employed. This allows useful experiments to be run in hours or days rather than years. The way in which these choices affect the physics of diffusion (including an increased advection and thermodiffusion contribution) is discussed in Section 5.6.1.

The surface of Mars experiences substantial diurnal and annual variations in surface temperature. The mean annual vapor pressure experienced by ice within the top few thermal skin depths will be biased toward higher pressures at shallower depths due to the nonlinear dependence of vapor pressure on temperature. This gives rise to a gradient which will pump water vapor into the subsurface if the atmospheric vapor density is above that at equilibrium with ice at depth. Rather than employing a varying surface temperature to create a gradient, the laboratory setup instead uses a constant thermal gradient across the sample. The resulting large gradient in vapor density permits the rapid growth of ice.

A rough analytical approximation to the rate of ice growth may be obtained by assuming D is independent of depth, and thus $\partial\sigma/\partial t$ is proportional to $\partial^2\rho_1/\partial z^2$, according to Equation (2.26). Using the Clausius-Clapeyron expression for vapor pressure, the second derivative of the vapor density gradient may be approximated by

$$\frac{\partial^2}{\partial z^2}\left(\frac{p_{sv}}{T}\right) \approx \frac{p_{sv}}{T}\left[\left(\frac{H}{RT}\right)^2 - 4\frac{H}{RT} + 2\right]\left(\frac{1}{T}\frac{\Delta T}{\Delta z}\right)^2, \tag{5.1}$$

for a linear temperature gradient. Here, H is the enthalpy of sublimation and R the universal gas constant. This simple scheme assumes that D is also independent of time; hence it does not include pore constriction.

Converting Equation (5.1) to density using the ideal gas law, the time necessary to achieve significant accumulation of ice in a laboratory setup, $\sigma/\dot{\sigma}$, may be estimated. Since the temperature gradient enters quadratically in Equation (5.1), a strong temperature gradient is clearly desirable for experiments.

Figure 5.1 plots contours of the number of days required to achieve complete pore filling using $\Delta T/\Delta z = 13$ K cm^{-1} and an ice-free diffusivity of 4.7 cm^2 s^{-1}. The figure reveals a parameter window where significant ice volume accumulates within days. The pore filling times are underestimates for any given set of conditions since this model does not incorporate pore constriction, but it clearly shows the time advantage gained by operating at higher temperatures. Lower pressure accelerates the growth because of higher diffusion coefficients, but once the Knudsen regime is reached, the mean free path of molecules no longer increases with decreasing pressure. Overlying the contours are the conditions of mean annual temperature and pressure on Mars' surface today, the conditions in this experimental setup, and the conditions in the Dry Valleys of Antarctica.
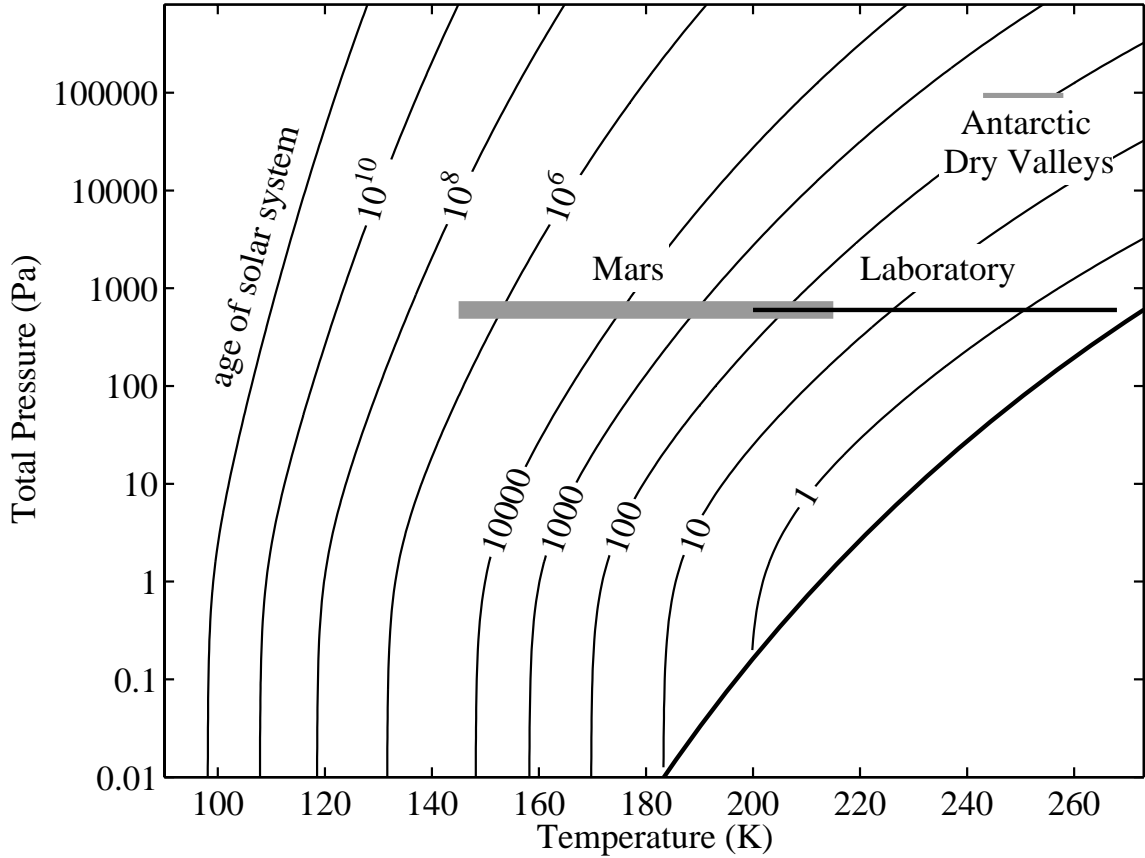
Figure 5.1: Contours of time in days to deposit a quantity of ice equivalent to 42% porosity for a temperature gradient of 13 K cm^{-1} using the simple model developed in Section 5.2 which assumes no constriction. The diffusivity of the simulant (500 μm glass beads) is extrapolated to appropriate temperatures and pressures using the Fickian formalism, which gives $D \propto p^{-1}T^{3/2}$. The heavy black curve is the saturation vapor line. The range of conditions on the surface of Mars, in the Dry Valleys of Antarctica (*Doran et al.*, 2002), and the experimental setup are indicated by horizontal bars. Note that the assumed temperature gradient for the laboratory experiments do not apply in these environments and that the growth rates would therefore be slower.

5.3 Experimental

5.3.1 Environmental control

Experiments were conducted at the Mars Simulation and Ice Laboratory at Caltech. A custom built stainless-steel vacuum chamber from LACO Technologies was used to achieve Mars-like pressures and a controlled humidity environment. The environmental chamber is a vertical cylinder with a removable lid, viton O-ring seals, and multiple electrical and fluid feedthroughs. The volume of the chamber is 2.3×10^{-2} m^3. Important environmental parameters which are controlled through the course of an experiment are the chamber pressure, atmospheric vapor density, and the top and bottom boundary temperatures of the sample column. These are maintained through 5 simultaneously operating PID control loops.

A schematic of the complete experimental setup is presented in Figure 5.2. Several interacting systems work to control the atmospheric vapor density and total pressure in the chamber. A vacuum pump continuously evacuates the chamber during an experiment and the pumping speed can be manually adjusted by a needle valve in the vacuum line. Evacuation is compensated by input of a controlled mixture of dry and humid CO_2. To create humid CO_2, dry CO_2 is passed through a mass flow controller (PID loop #1) and a sparger into a 5 L vessel of distilled, deionized water. The temperature of the water in this bubbler is maintained at 38° via PID control (loop #2) of a hemispherical heating mantle. The gas output of the bubbler leads to the main chamber. Pressure in the bubbler is forced down by the evacuation of the main chamber but is maintained at approximately 60 mbar by PID loop (#3) actuation of the dry gas input which feeds the bubbler. By maintaining a constant bubbler temperature and pressure, the vapor content of the head space gas in the bubbler is maintained to within about 10%. The bubbler pressure is kept slightly bellow the boiling point of water so that the head space gas has a high water content (typically ∼85–90% relative humidity at 30°C). This humid gas is fed into the main chamber through a mass flow controller optimized for regulating low-pressure flows. This MFC is also under PID control (loop #4) where a humidity sensor (described below) provides input to the loop by measuring the vapor density of water at the sample surface. A heating tape around the gas line from the bubbler prevents water from condensing before it reaches the chamber. A third mass flow controller regulates the input of dry gas into the main chamber (loop #5). The low-pressure MFC control loop (#4) first adjusts the input of humid gas to achieve the desired chamber vapor density. The dry gas loop (#5) then brings the total chamber pressure to 6 mbar. Pressure feedback between these two loops is rapid and settles within ∼5 minutes to a steady state which can be tuned so the controllers are far from saturation.

In this experiment, as much water as possible is removed before introducing sub-zero temperatures. Porous media simulant which has been kept dry in an oven at 400 K is cooled to approximately 320 K in a desiccator and then poured into place in the sample chamber. The chamber is then sealed and pumped down to 600 Pa and maintained with dry CO_2. The sample surface is maintained at 320 K by a halogen lamp until the measured vapor density drops below 0.1 g m^{-3}, usually several hours. Any water remaining in the chamber when the cold plate is activated is quickly gettered onto the lowest level of the soil. The low vapor densities measured in the cold, dry chamber suggest that any ice present when the chamber is opened to humid gas should only persist in the bottom 1–2 cm of the sample where the soil is ≲220 K, and it is later shown that this amount of ice is negligible.

The sample column is chilled from its base via a copper cold plate. A methanol recirculating chiller acts to keep the cold plate at 183±1 K. Thermal losses through silicone grease connecting the cold plate and the contact plate attached to the sample caddy results in a sample base temperature of approximately 193±2 K. The cold plate, cooling lines, and all other cold surfaces in the chamber are coated with polyurethane foam to slow heat conduction and prevent gettering of atmospheric
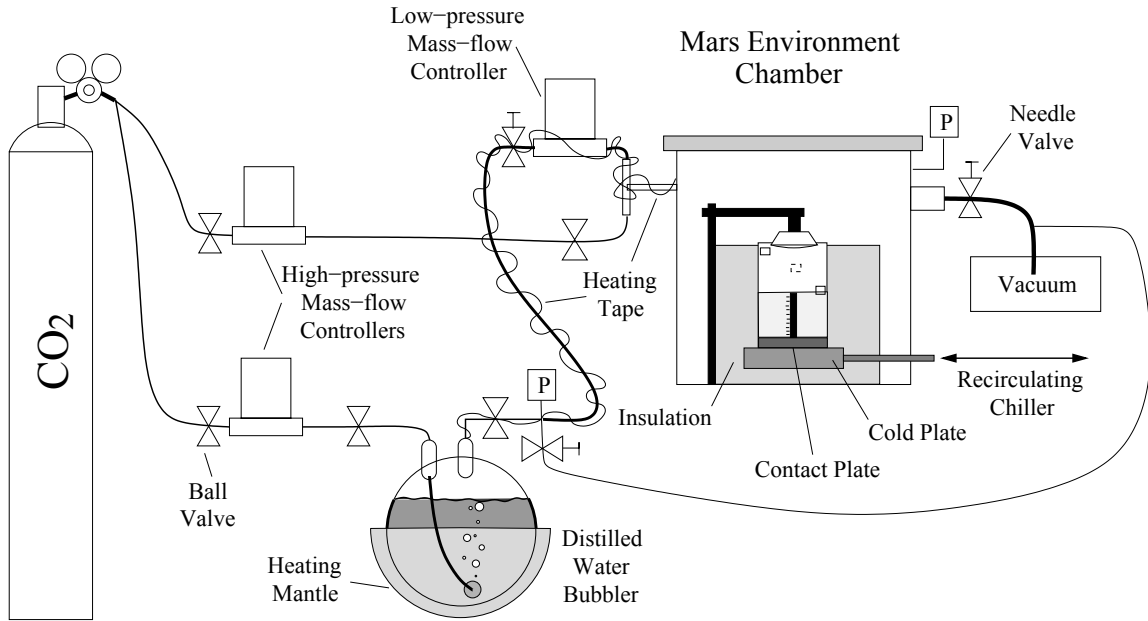
Figure 5.2: Schematic of experimental setup highlighting gas humidification and delivery, and pressure control. The sample container within the environment chamber at right is expanded and annotated in Figure 5.3. The datalogger and electrical interface connections are not shown.

water in locations other than the soil column. The surface of the sample is maintained at 268 K via another independent PID loop controlling a halogen lamp and reflector placed approximately 6 cm above the sample surface. The input for the lamp controller is the surface temperature as measured by the uppermost thermocouple of the sample thermal probe described in the next section.

5.3.2 Sensors

The pressure in the main chamber is monitored using an MKS Baratron 626 capacitance manometer with a full-scale range of 10 torr. The pressure in the bubbler is monitored with an MKS 902-series piezo-transducer, with a full range of 1000 torr.

Water content of the chamber atmosphere is monitored using RH/RTD sensors (Honeywell model HIH-4602-C) which simultaneously report relative humidity (RH) and ambient temperature at the sensor via a platinum resistance temperature device (RTD). The ITS-90 formulation (*Hardy*, 1998) is used to convert the relative humidity into a partial pressure of water. Vapor density is calculated via the ideal gas law using the measured RTD temperature.

Temperature as a function of depth is monitored with a custom temperature probe. The probe consists of 11 T-type thermocouples which protrude at half-centimeter intervals from a perforated plastic tube. The sensing ends of the thermocouples are approximately one half centimeter from the plastic body of the sensor assembly and are held in place with a fin of kapton tape. This arrangement minimizes the effects of vertical heat transport through the sensor body to the thermocouple heads

and allows each thermocouple to be in close equilibrium with the local thermal environment.

The data from an experiment are recorded with a National Instruments Compact DAQ–9172 datalogger. All process variables are monitored throughout an experimental run at approximately three-second intervals. Averaging of these data is performed every minute and the averages are logged. Since all process variables change slowly, this does not compromise the integrity of the dataset.

5.3.3   Sample preparation and method

The porous medium used in all experiments is composed of soda lime glass beads obtained from AGSCO Corporation (mesh size #30–40). The mean particle size is 500 μm, no more than 10% larger than 700 μm and no more than 20% smaller than 400 μm (AGSCO technical data sheet). The density of the glass is 2.5 ± 0.1 g cm^{-3}. The diffusivity of these beads were measured using the techniques of *Hudson et al.* (2007) under 586 Pa CO_2 at 250 K, and was found to be 4.7 ± 0.5 cm^2 s^{-1}. The glass beads' size place them in the sedimentological category of "coarse sand".

The sample caddy is a thin-walled squat plastic cylinder $\sim$7.5 cm in diameter, the base of which is a snugly fit brass contact plate (see Figure 5.3). Oven-dried simulant is poured into the caddy to a depth of 5 cm. The temperature probe is then inserted through the sample and the relative humidity sensor is positioned such that it penetrates the surface of the soil by a few millimeters. The tops and exposed wires of the sensors are wrapped in aluminum foil to reduce heating by the halogen lamp.

The chamber is sealed and evacuated to 600 Pa and maintained at this pressure with input of dry CO_2 for several hours to remove residual water. The recirculating chiller is then activated and the sample is cooled for at least 6 hours until the sample temperature profile reaches steady-state. At all subsequent times the temperature profile is close to linear, but changes in sample thermal conductivity due to ice deposition and heat losses through the caddy walls result in minor deviations following exposure to humid gas. Once thermally equilibrated, the humid CO_2 line is opened and the humidity stabilizes at the desired value.

At the conclusion of the experiment, the chamber is purged and the ice-bearing sample and caddy are extracted to a 260 K freezer. The sample caddy is affixed to a custom extrusion device and the sample is sliced horizontally at half-centimeter intervals. Each layer is removed by scraping and brushing (in the case of poorly consolidated soils) or sawing (in the case of ice-rich soils), and collected in a glass beaker. Samples from each layer are immediately weighed, giving a total mass (ice + simulant), m_t. Beakers of ice-bearing sample are then placed into an oven at 390 K for a minimum of 24 hours. The dried samples are cooled to freezer temperatures in a desiccator. They are weighed again at the same temperature as the ice-bearing samples to obtain the dry simulant mass per layer, m_s.
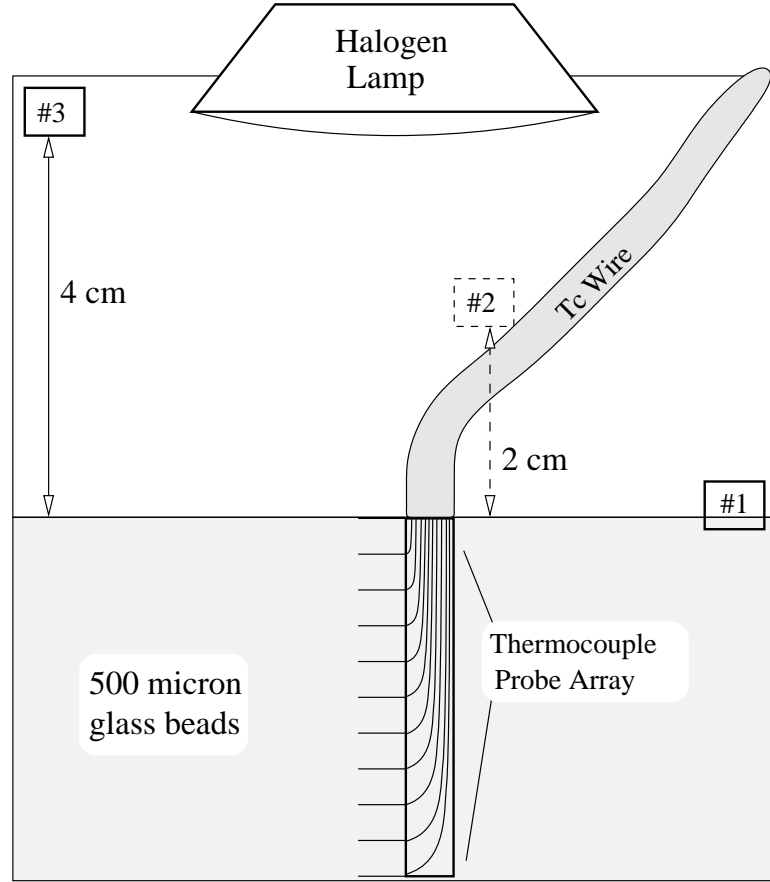
Figure 5.3: Schematic of sample container. Numbered boxes are positions of RH/RTD sensors. Sensor #1 has its sensing face buried $\sim$2 mm beneath the sample surface. Sensor #1 and Sensor #2 (against the back wall of the cylindrical caddy) are directly illuminated by the lamp. Sensor #3 is not directly illuminated, but is in close proximity to the lamp reflector. Thermocouple leads are wrapped in aluminum foil and cast a shadow over part of the sample surface.

5.3.4 Data analysis

Difference in mass before and after baking is the gravimetric water content. The combined height of all samples measured at the conclusion of the experiments is within $\sim$1 mm of the pre-experiment values, indicating negligible bulk expansion. For 500 μm glass beads, the bulk density is determined to be $\rho_{\mathrm{bulk}} = 1.46 \pm 0.01$ g cm^{-3}. Layer thicknesses are calculated from the measured mass of dry soil as $\delta z = m_s/(\rho_{\mathrm{bulk}}A)$, where δz is the thickness of layer z, and A is the area of the sample caddy.

Over the range of temperature encountered in this experiment, the density of bulk ice varies by $\sim$1%, and it is assumed that all deposited ice has a density of $\rho_{\mathrm{ice}} = 918$ kg m^{-3}. The mass of water per layer allows the calculation of ice density relative to free space, $\sigma = m_w/v = (m_t - m_s)/(\delta z A) = \rho_{\mathrm{bulk}}(m_t/m_s - 1)$, where m_w and v are the mass of ice and the total volume in a given layer. The maximum possible ice density relative to total sample is $\sigma_0 = \phi_0\rho_{\mathrm{ice}}$, where ϕ_0 is the ice-free porosity and ρ_{ice} is the density of pure ice, and thus the filling fraction is σ/σ_0.

Duration, [hrs]	ρ_1, [g m^{-3}]	Max filling, [%]	z_{ice}, [cm]
0	1.60	0±1	0
6	1.60	11±2	1.1
12	1.60	15±3	0.6
18	1.60	21±2	0.2
24	1.60	29±3	0.1
24	1.60	29±3	0.1
24	1.60	26±3	0
24	1.60	29±3	0
48	1.60	42±3	0
48	1.60	43±3	0
72	1.60	54±4	0
72	1.60	55±4	0
96	1.60	64±5	0
96	1.60	76±4	0
98	1.60	71±9	0
120	1.60	65±4	0
122	1.60	71±5	0
331	1.60	75±5	0
530	1.60	90±4	0
24	0.60	10±2	2.2
24	0.85	13±2	1.8
24	1.10	21±2	0.5
24	1.35	26±3	0.1

Table 5.1: List of experiments. z_{ice} is ice table depth; a value of 0 denotes surface ice.

A control experiment was run to test the degree of ice accumulation during sample analysis. A sample was prepared in the same manner as other samples, but was never exposed to a humid chamber atmosphere. The amount of water collected by the sample during analysis is less than 0.4% filling fraction, negligible compared to all non-zero experiment times.

5.4   Results

Experiment durations, target surface vapor densities and observed ice table depths are given in Table 5.1.

5.4.1   Diffusive ice morphology

The deposition of ice in porous media at conditions below the triple point of water experimentally demonstrates ice-vapor diffusion and deposition in the absence of a liquid phase. Significant deposition occurs at all sample depths, indicating vapor diffusion as the primary mechanism for H_2O transport. Though quasi-liquid films may be present under these conditions in the shallow (T>250 K) regions of the sample (*e.g., Elbaum et al.*, 1993) they would be discontinuous or absent at greater depths with lower temperatures.

Small chips of ice-encrusted beads from several sample depths were examined with an optical microscope in the cold room; Figure 5.4 displays selected images. Figures 5.4 a and b show ice necks connecting individual beads to a larger bulk mass of beads and ice. The necks form annuli around grain contacts, the edges of which are concave toward the contact (see panel b). The shape and location of these necks is consistent with ice growth models based on free-energy arguments (*Hobbs and Mason*, 1964). Panel c shows turbid ice filling the interstices between several beads. Monocrystalline ice should not significantly scatter light and would appear clear; the turbidity implies the presence of crystalline defects or included air. Panel d shows a socket formerly occupied by a bead, revealing the tight association and good thermal contact between ice and the grains of the medium.

Panels e and f reveal bubbles within the ice which are tens of microns across. Spread throughout the sample, such voids could measurably reduce the bulk density of the ice. Though trapped atmospheric gases are common in compressed snowpack ice, their occurrence in diffusively derived ice has not been commented on previously. It thus seems that future landed missions which seek to extract information about ancient climates and atmospheres would be able to find trapped pockets of relic gases in subsurface ice even if that ice were not the result of precipitation.

5.4.2   Ice table morphology

Recent modeling investigations into subsurface ice deposition on Mars have shown that the ice table itself is a sharp boundary between ice-bearing and ice-free soil (*Schorghofer and Aharonson*, 2005). These results differ from earlier models of *Mellon and Jakosky* (1993) which exhibit a more gradual transition spanning several model layers. *Schorghofer and Aharonson* (2005) suggest that the difference may be due to differences in numerical implementation, rather than different physics or underlying assumptions. The experiments reported here exhibit sharp interfaces, the depth and morphology of which are controlled by temperature and atmospheric vapor density. In experiments which develop ice tables beneath the sample surface the mechanical cohesion of the beads exhibits a transition between completely unconsolidated and well-bound over a distance of order one grain diameter.

Because of this sharpness, the ice table shape may be easily seen by brushing away the unbound beads and examining the surface of ice-cemented grains. Figure 5.5 shows one such example: an experiment where some surface ice developed in the colder shadow of the thermocouple wires, but where there remained some warmer, unshadowed beads not yet bound by ice. The top of the RH/RTD sensor is directly illuminated by the lamp and experiences a temperature 5–15 K warmer than the sample surface. This produces a small depression in the ice table which is ∼1 mm larger than the sensor diameter. A minor deepening of the ice table exists at the walls of the sample due to heat leakage from the caddy. The ice table is nearly flat in regions not perturbed by shadows,
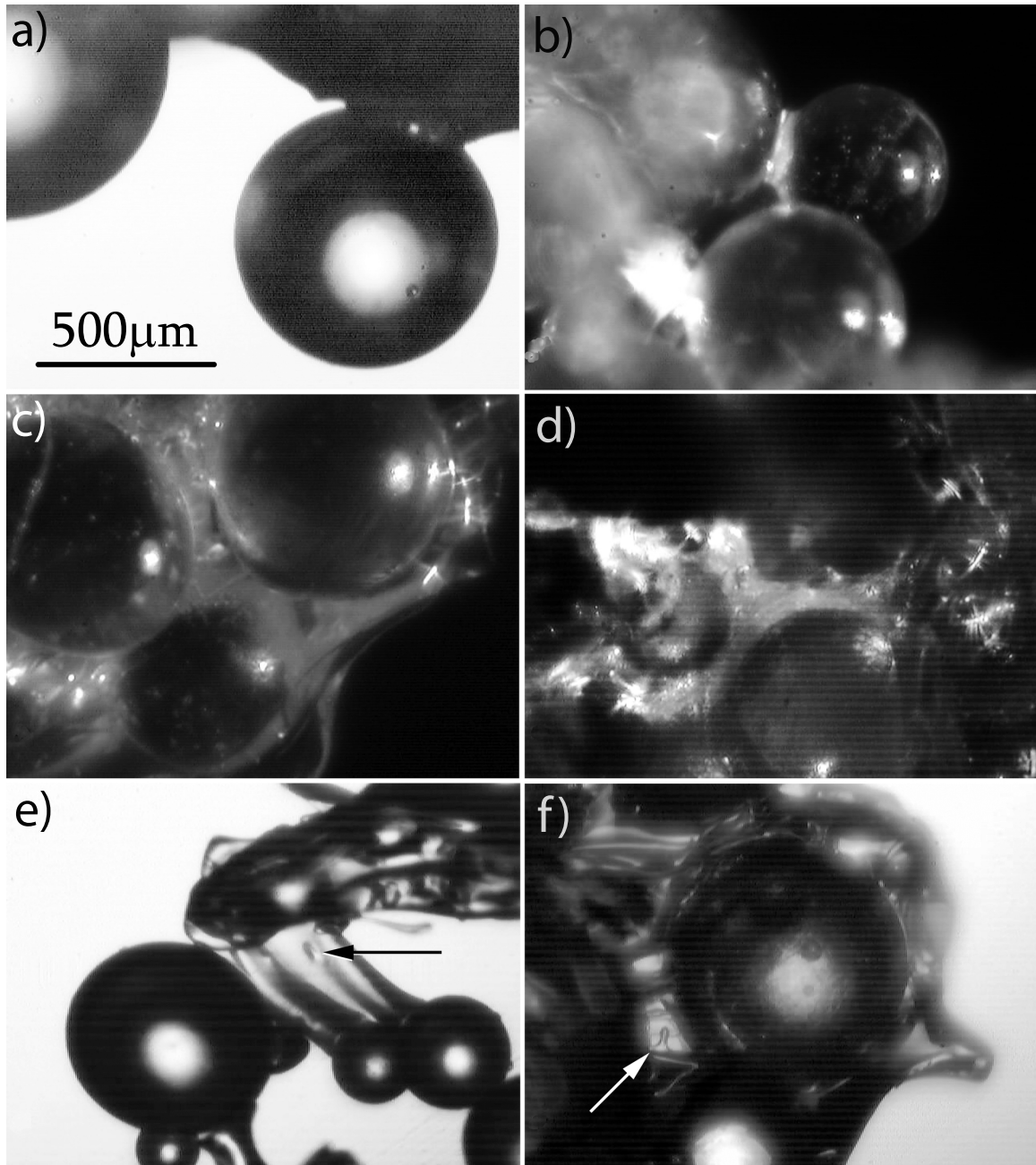
Figure 5.4: Images of the porous medium (500 μm glass beads) after exposure to experimental conditions. Images a, e, and f are back-lit; the scale bar applies to all images. Images a–c are from the 331 hour experiment, d–f are from a 72 hour experiment; all were performed at a nominal vapor density, monitored by sensor #1, of 1.6 g m^{-3}. a–b) Ice necks holding beads in place. Neck shapes are consistent with predictions of ice nucleation and growth based on surface energy. c) Beads embedded in pore-filling ice; the cloudy appearance suggests the presence of air bubbles or other defects. d) Sockets of ice formerly occupied by beads. e–f) Fine necks and pore-filling ice, respectively. Air bubbles trapped within the ice are indicated by arrows.

a) Before brushing

b)
Loose Beads

Ice and Beads at Surface

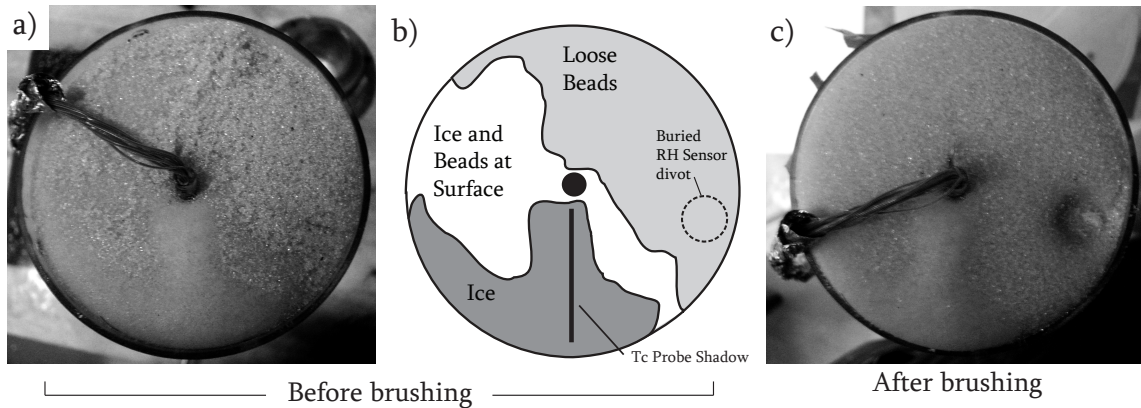Buried RH Sensor divot

Ice

Tc Probe Shadow

c) After brushing

Figure 5.5: The sample surface after 96 hours of exposure to a humid atmosphere. a) The surface as it appeared prior to brushing. b) Schematic indicating a region of free surface ice, an intimate ice and bead mixture, and a region with multiple layers of ice-free beads. The position of the thermocouple wire shadow is indicated. c) The surface after brushing away loose beads, revealing the divot formed around the warm RH/RTD sensor.

edge effects, or the warm sensor, with depth variations less than 1 mm across several cm of surface. Such a uniform depth of the stability boundary indicates a radially uniform temperature profile with isotherms parallel to the surface.

On Mars, patches of darker or brighter dust will experience different radiative equilibrium temperatures for the same amount of insolation. *Sizemore and Mellon* (2006) have examined the consequences of this phenomenon with two- and three-dimensional numerical models. The effects of spatial variations in albedo on the near-surface ice table morphology have been experimentally examined with this facility. A gold-coated disk (albedo $\approx$1.0), a matte black disk (albedo $\approx$ 0.1–0.2), and an unaltered, clear disk (control) were placed on the sample surfaces to produce local temperature perturbations. An image of disk placement is in Figure 5.6 a). Samples were chilled and exposed to a humid atmosphere for 48 hours. A T-type thermocouple epoxied to the underside of each disk measured equilibrium temperatures of 263.1 K, 270.8 K, and 268.2 K, for the gold, black, and control disks, respectively. The clear control disk temperature is within 0.1 K of the glass beads (268 K). Following exposure, the disks were removed and the depth to the ice table was measured. A wire mesh placed above each sample defined the positions for $\sim$1100 individual staggered-grid depth measurements performed with a needle graduated at 1 mm intervals. These measurements were then interpolated to produce the depth maps seen in Figures 5.6 c and d.

To produce the ice table in Figure 5.6 d, the vapor density at the sample surface was set at a nominal value of $1.6\,\mathrm{g\,m^{-3}}$. As can be seen from both the photograph taken with oblique illumination (Figure 5.6 b and the depth map (5.6 d, the ice table exhibits significant undulations in depth on a scale comparable to the radius of the albedo disks. The depth to the ice table around the rim of the high-albedo disk is the shallowest observed ($\sim$0.3–0.4 cm). In the vicinity of the low-albedo disk,
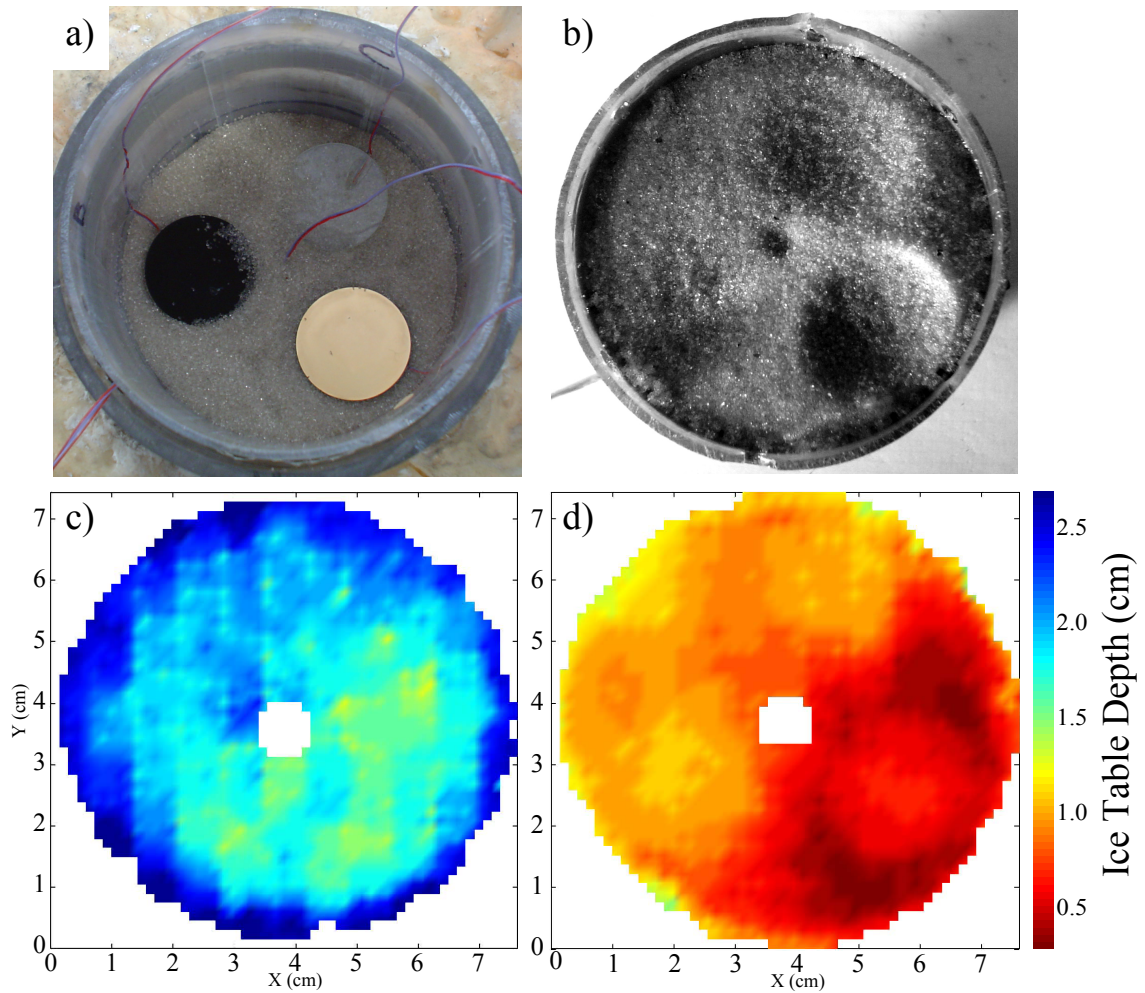
Figure 5.6: Experiments illustrating the effect of surface albedo on ice table development. a) Albedo disk placement on sample surface. b) Ice table for high vapor density case ($\rho_{\text{air}} = 1.6$ g m^{-3}), photographed with oblique illumination from the lower left. c) Ice table depth map for the low vapor density case ($\rho_{\text{air}} = 0.6$ g m^{-3}). d) Ice table depth map for high vapor density case ($\rho_{\text{air}} = 1.6$ g m^{-3}). Both experiments were exposed to a humid atmosphere for 48 hours.

the depth to the ice table is on the order of 1 cm due to isotherm depression by the warmer disk. The clear albedo disk had a smaller effect on the local environment.

An interesting effect of the high-albedo disk is the rim of shallow ice which gives way to a depression beneath the center of the disk. A possible explanation is inhibited vertical diffusion of water vapor due to the impermeable body of the disk, and the curved isotherms beneath it. Vapor moving laterally underneath the disk encounters temperatures where the vapor is saturated (an upwards deflection of the equilibrium ice table), and deposits. Vapor densities in the cold regions under the central portion of the disk are thus small and insufficient to deposit ice.

An experiment with an identical setup and duration but less than half of the atmospheric vapor

density (ρ_{air} = 0.6 g m^{-3}) was performed, and the depth map is shown in Figure 5.6 c. The lower vapor density resulted in a slower upward migration of the ice table. After 48 hours, the mean depth is 2±0.1 cm, compared to 0.8±0.3 cm for the experiment at higher humidity. At lower humidity, the ice table topography is subdued: the effect of the high-albedo disk is still seen over approximately half of the disk's surface, but the central depression effect and the discernible outline of the disk itself are absent. The greater thickness of low thermal conductivity ice-free beads insulates the ice table from the temperature perturbations at the surface. On Mars as in these experiments, the ice-free regolith above the ice table will rapidly attenuate temperature heterogeneities, reducing the sensitivity of ice-table morphology to surface albedo variations as a function of depth.

5.4.3 Ice table depth

To explore the depth of the ice table, several experiments were run for 24 hours with different values of atmospheric vapor density. Figure 5.7 shows the results of eight experiments, four run at the nominal vapor density of 1.6 g m^{-3}, and four at reduced chamber humidities.

The depth of the ice table and the total quantity of ice deposited in a given time depends sensitively on the atmospheric vapor density. The equilibrium ice table depths for the vapor densities 0.6, 0.85, 1.1, 1.35, and 1.6 g m^{-3} under a 13 K cm^{-1} gradient and a surface temperature of 268 K are, respectively, 1.4, 1.1, 0.92, 0.75, and 0.61 cm. Initially, significant ice is deposited several centimeters below the equilibrium depth. Higher vapor densities allow earlier ice deposition at a given level. Once ice has deposited, local temperature gradients in the ice control vapor flux, and the deep ice becomes isolated from the atmospheric vapor content. Experiments with high value of ρ_{air} (1.1–1.6 g m^{-3}) experience early deposition at depth and subsequently evolve at similar rates. Thus, the data for such experiments overlap between the base and ∼3 cm in Figure 5.7. The phenomenology of the early transients in ice deposition is examined further in Section 5.6.4.

5.4.4 Ice profile

The structure of the ice distribution beneath the ice table, in a region which may be termed the cryosphere, is revealed in these experiments as a function of both depth and time and is interpretable in terms of the experimental conditions and durations. The water contents determined from gravimetric analysis reveal profiles of ice content which decrease monotonically below the depth of maximum filling. Low humidity or short-duration experiments give rise to an ice table beneath an ice-free layer, while other conditions (*e.g.*, longer durations, higher vapor densities) produce stable surface ice. Figure 5.8 plots the final ice content results of experiments run for different periods of exposure to an atmosphere with a surface vapor density (reported by sensor #1) of 1.6 g m^{-3}. As described in Section 5.5.2, the actual vapor density driving the flux of water is believed to be
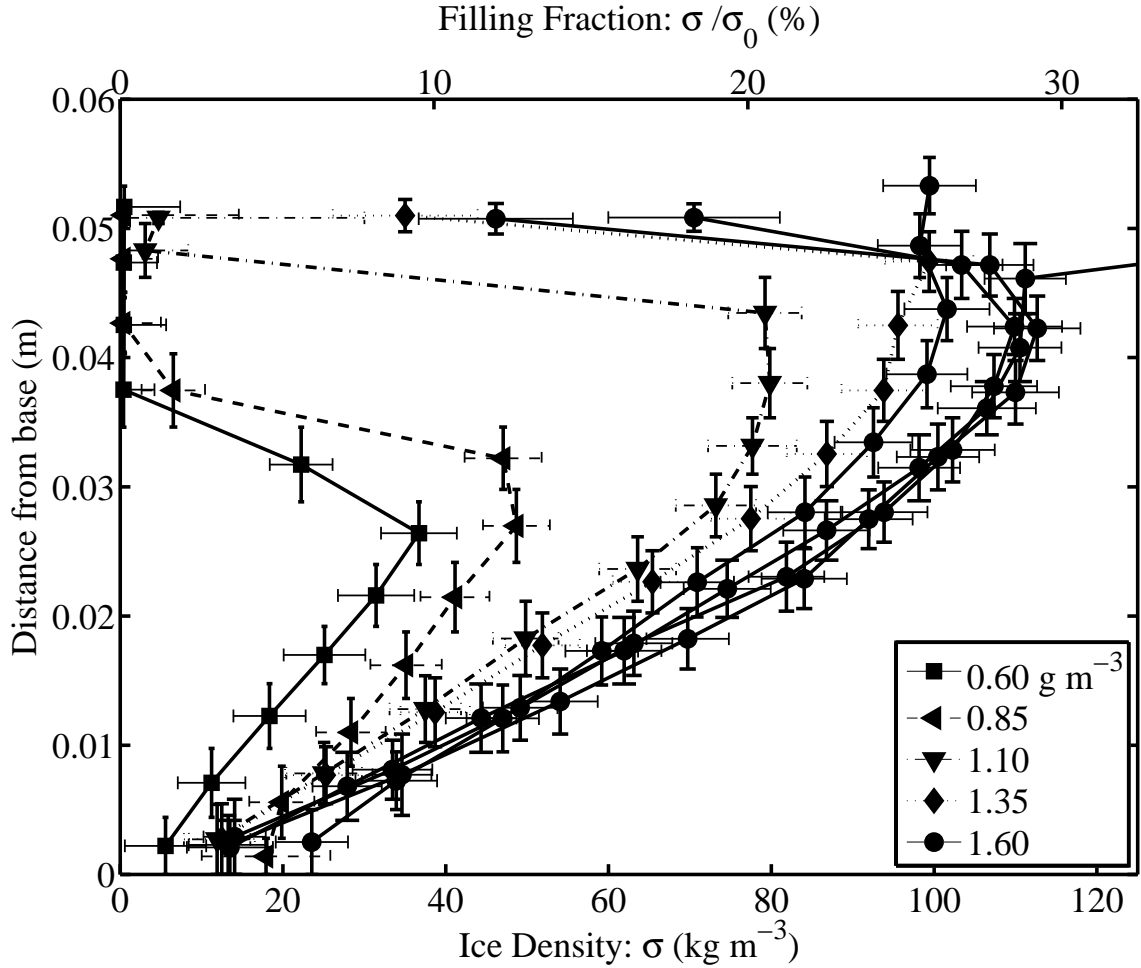
Figure 5.7: Ice content data for experiments run for 24 hours at various vapor densities. Ice contents are reported as density of deposited ice with respect to total volume (σ) and fraction of pore space filled with ice, assuming a constant ice-free porosity of 42%. The maximum density of ice is thus $\phi_0 \rho_{\text{ice}} = \sigma_0 = 385.6$ kg m^{-3}

somewhat higher. The maximum filling fraction observed, approximately 90%, was observed at the end of the longest duration experiment.

As revealed in Figure 5.8, the ice contents first increase rapidly, followed by a reduced rate of ice accumulation. The shortest experiments were performed in additive 6-hour increments, the second set's durations were 24 hours apart, and the final long-duration experiments are 110 hours and 199 hours longer than the next shorter runs.

5.4.5   Constriction

In a porous regolith, the free-gas diffusion coefficient is reduced by a factor proportional to the cross-sectional area of the medium. An equivalent diffusivity, D, may be written in a regime which involves both molecule–molecule collisions and collisions with the pore walls to a significant degree.
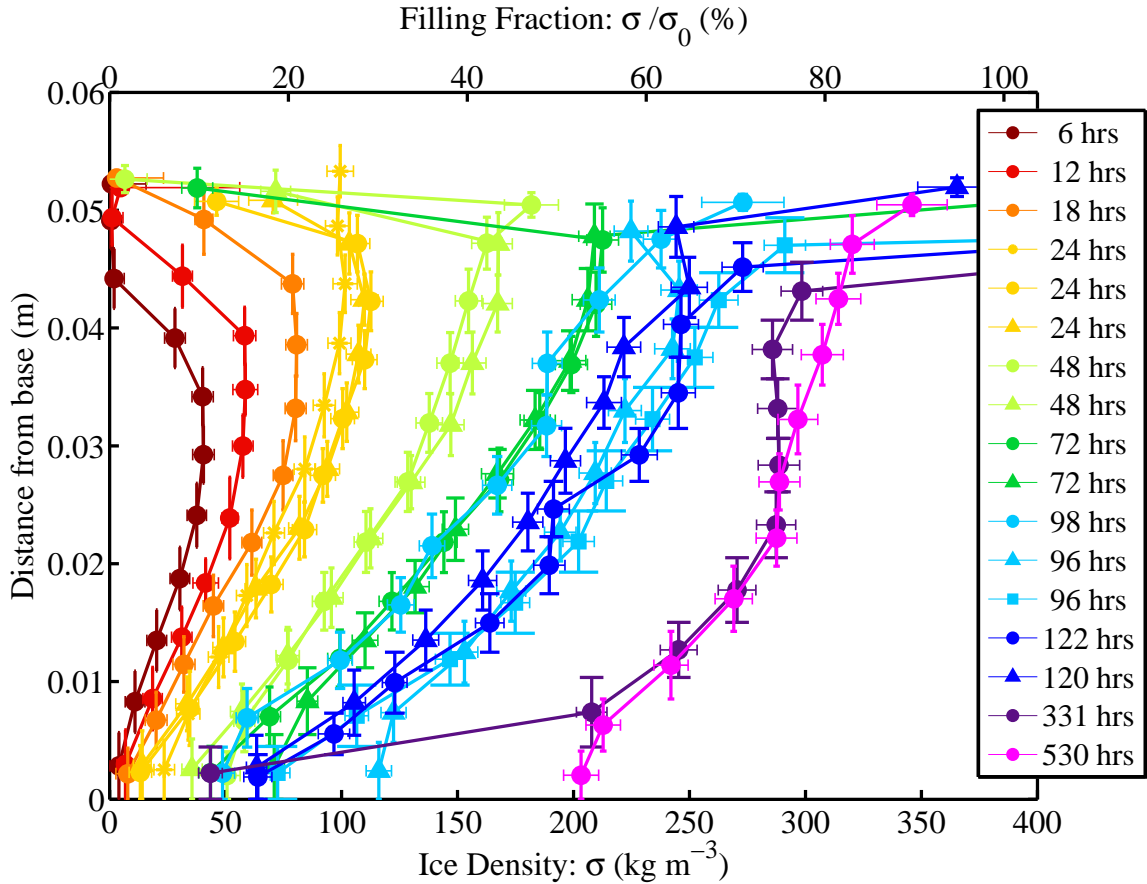
Figure 5.8: Ice content data for experiments run at a nominal surface vapor density of 1.6 g m^{-3} and various durations. After $\sim$48 hours, free ice deposits at the surface and forces the uppermost point for some samples to have a measured ice content offscale to the right. The colors correspond to duration of exposure to a wet atmosphere, as indicated by the legend. Experiments with similar durations are given the same color, but different symbols.

This is given by the Bosanquet equation,

$$\frac{1}{D} = \frac{1}{D_F} + \frac{1}{D_K},\tag{5.2}$$

where D_F is the Fickian diffusivity, which dominates when collisions between gas molecules dominate the behavior of the gas movement, and the Knudsen diffusivity D_K which dominates at low pressures when molecules collide more frequently with pore walls than with each other (*Pollard and Present*, 1948). As ice accumulates, the pore space geometry changes, altering the porosity and tortuosity, and increasing the frequency of molecule–wall collisions as the pore size is reduced. D_F and D_K depend upon the pore geometry in potentially different ways. These effects are examined further in Section 5.6.2.

As described in the previous section, the rate of ice growth throughout the column is not uniform due to the non-linear gradient in vapor pressure at depths where ice is present. Initially, ice grows
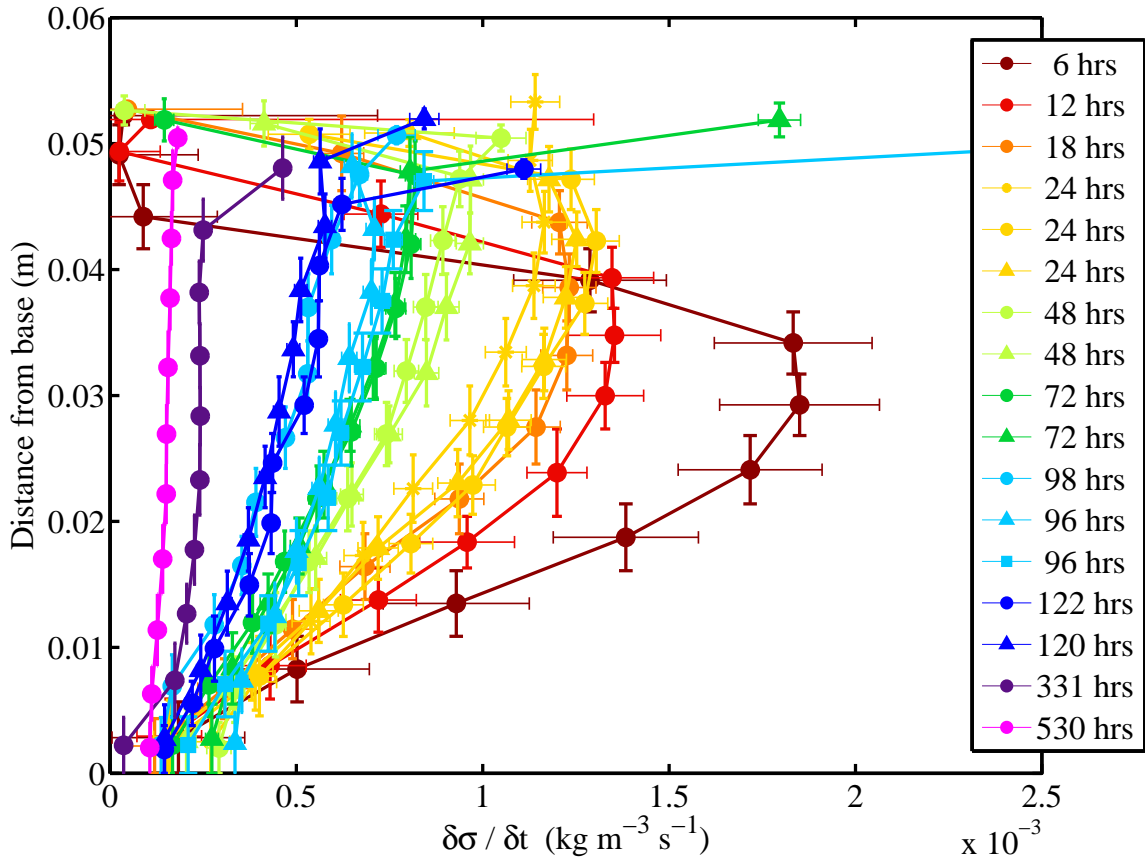
Figure 5.9: The change in ice content for a given depth divided by the time interval for growth. The legend (distinct from Figure 5.8) indicates the end of the time interval (*e.g.*, "6 hours" is 0–6 hours, "48 hours" is 24–48 hours, etc.). The most rapid ice growth occurs during the earliest times of exposure (0–6 hours), and the maximum can be seen to evolve from a depth $\sim$2.0 cm for 0–6 hours to $\sim$1.0 cm for 6–12 hours, to the surface for times between 12 and 24 hours. Subsequent to this, the rates are much smaller, are much more uniform across the sample depth, and continue to decrease with time.

most quickly at the top of the ice table where the vapor density gradient is steepest. Beneath the ice table the rate of ice growth also varies with time due to the effect of constriction. This may be seen in the spacing of the contours in Figure 5.8, but is more clearly evident in Figure 5.9, where the difference in ice contents between successively timed experiments are divided by the intervals between those experiments, thus plotting the incremental change in ice content, $\delta\sigma/\delta t$. Similarly timed experiments are differenced from an experiment of significantly shorter ($>$5 hours) duration.

Figure 5.9 reveals the depth of greatest ice growth in a given time increment. For the first 6 hours (dark red), most ice deposits between 1.5–2.5 cm beneath the surface. In the next longer increment, from 6–12 hours (bright red), the greatest growth is at about 1.0 cm depth. Between 18 hours to 48 hours (orange and yellow), the greatest ice deposition occurs in the uppermost soil layer. At all subsequent times, the ice growth progresses more uniformly with depth, but accumulation rates

decrease as exposure time to a humid atmosphere continues to increase.

5.5 Numerical Model and Experiments

5.5.1 Description of ice-filling model

Vapor transport and phase transitions are calculated with the numerical code described in *Schorghofer and Aharonson* (2005), which is used to model the experiments presented here. Fick's law, local mass conservation, and the ideal gas law lead to

$$\frac{\partial}{\partial t}\left[\left(\phi_0 - \frac{\sigma}{\rho_{\text{ice}}}\right)\frac{p_1}{T} + \frac{R}{18}\sigma\right] = \frac{\partial}{\partial z}\left[D\frac{\partial}{\partial z}\frac{p_1}{T}\right], \tag{5.3}$$

where p_1 is the partial pressure of H_2O. Within the ice-containing region the ice growth can also be obtained from Equations (2.26) and (5.1), but these equations do not directly provide the vapor density in a dry layer or the depth of the ice interface. Hence, the partial differential equation (5.3), which includes these effects, is used.

Equation (5.3) is numerically solved with an explicit forward-difference scheme, with a spatial resolution of 0.5 cm, the spacing of the temperature sensors in the experiment. Models may also be run with temperatures interpolated to a finer grid spacing. Experimentally measured temperature profiles and surface vapor densities are used as input. To remove artificial temperature inflections caused by thermocouple misalignment from exact half-centimeter spacing, the temperature data are fit with a 4th-degree polynomial prior to being used as input. Small time steps are required for numerical stability, and the program subdivides measured temperature profiles, typically available in 1 minute intervals, into smaller time steps of 50–1000 μs by linear interpolation.

5.5.2 Comparison to models and uncertainties

In this section five quantities are considered which impact the agreement of the model with the experimental ice contents. They are: headspace vapor density (ρ_{air}), ice-free diffusion coefficient (D_0), temperature profile, density of deposited ice (ρ_{ice}), and what is here termed the constriction exponent (n).

Experiments performed with three humidity sensors placed as indicated in Figure 5.3 recorded vapor densities consistently 80% higher at sensors #2 and #3 than at sensor #1. Additionally, ice was observed to deposit at the sample surface after ∼48 hours while the vapor density reported by sensor #1 implied an ice table ∼0.6 cm beneath the surface. It is therefore surmised that 1) the atmosphere above the sample in these experiments is not well mixed, and 2) the bulk atmospheric vapor density driving the flux of water vapor is higher than 1.6 g cm^{-3} by almost a factor of 2.

Compensation equations for sensor temperature are provided by the vendor; however the range of validity for those expressions may not extend to low-pressure environments.

This uncertainty in ρ_{air} affects estimates of ice table depth and ice contents in experiments of less than $\sim$48 hours duration. In Figure 5.10, the final ice content measured for a 24 hour experiment is displayed, along with results of numerical simulations using the model described in Section 5.5.1. All model runs use the subsurface temperature profile as recorded. When vapor densities reported by sensor #1 are used, the model underpredicts ice contents in the upper half of the sample (Figure 5.10, triangular symbols) compared to experimental data (filled circles, solid black curve). When vapor densities are prescribed constant values, models with higher surface vapor densities are seen to produce ice at shallower depths more akin to the experimental profile. The best match between models and experiments for exposure times less than $\sim$48 hours are with $\rho_{\mathrm{air}} =$2.0–3.2 g m^{-3}, lower values producing the best correspondence with the shortest times. For 48 hour experiments, good agreement between experiments and models is obtained for surface vapor densities of $\sim$3.2 g m^{-3}. This value is equal to the vapor density of ice at 268 K and 600 Pa, *i.e.*, the conditions maintained at the surface of the sample, and therefore suggests that free surface ice becomes the dominant vapor source.

An important feature of Figure 5.10 is that all model runs, despite differing surface vapor densities, agree beneath the depth where ice is present; the curves merge onto a single line. Flux beneath the ice table is governed by the local vapor pressure, which is controlled by temperature and is independent of the atmospheric vapor density. The important differentiation among models with different surface vapor densities is the time when a particular depth begins to deposit ice. Higher vapor densities advance this point to earlier times at a given depth.

In the rest of this section dealing with model and experiment agreement, the focus is primarily on runs of 48 hours or longer, and the discussion is therefore specific to experimental data and models run with surface vapor densities of 3.2 g m^{-3}. When such models are run, they consistently overpredict the abundance of ice in the sample, indicating that some other factor besides vapor density is acting to reduce ice deposition.

Measurements of D_0 for the 500 μm glass beads have an uncertainty of about 10% (Section 5.3.3). Additional model runs were performed using $D_0 = 4.2$ cm^2 s^{-1} to determine if reasonably lower values of D_0 would bring closer agreement with experimental results. Such models do exhibit reduced ice contents, but do not bring the model output into good agreement with the data. It is therefore concluded that the major source of variation lies elsewhere and $D_0 = 4.7$ cm^2 s^{-1} is used for subsequent model analyses.

A $\sim$1 mm vertical deviation in thermocouple placement results in $\sim$1 K temperature offset, corresponding to a 10% variation in vapor density at the highest ($\sim$268 K) experiment temperatures. Models run with imposed 1 K shifts to lower temperatures produced insignificant differences in ice
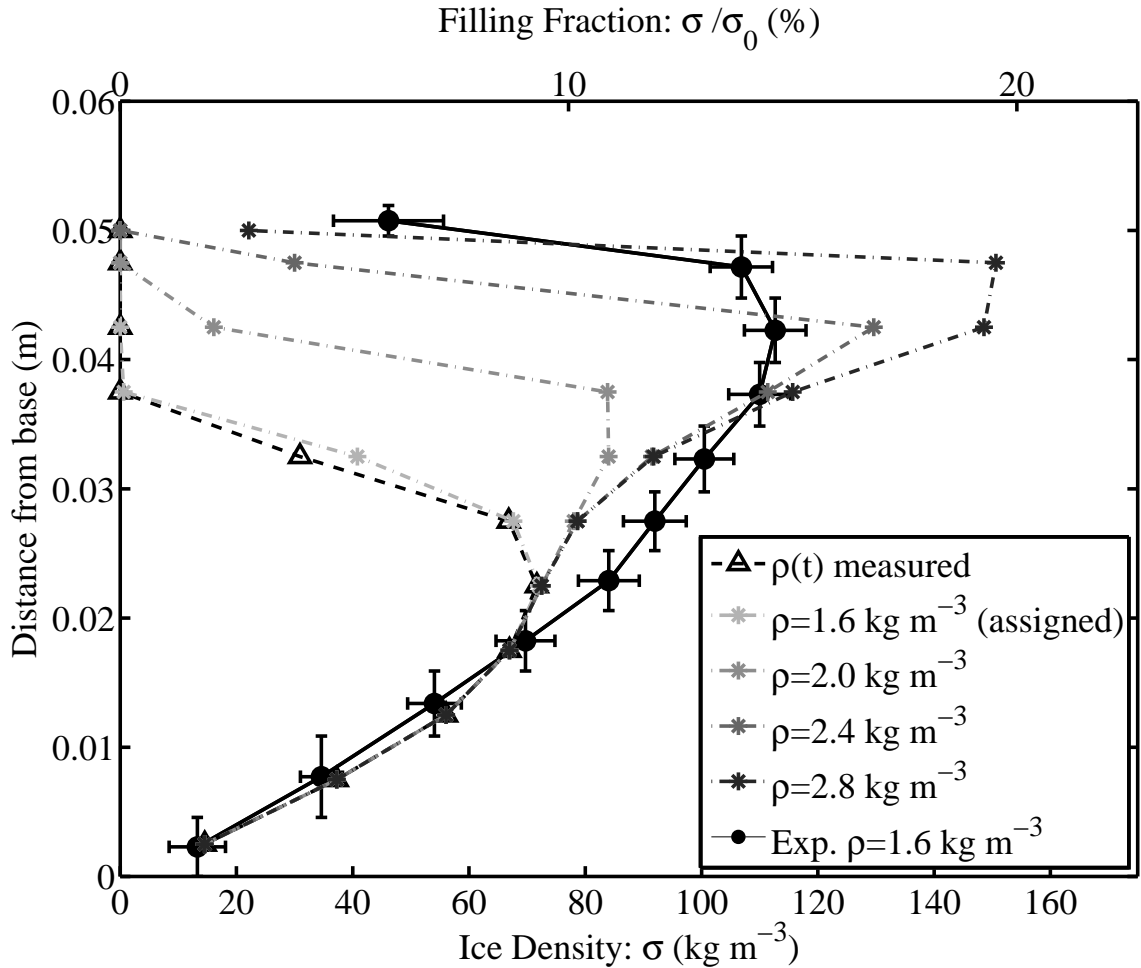
Figure 5.10: Ice content data for a 24-hour exposure experiment at a nominal measured vapor density of 1.6 g m^{-3} (black circles, solid line), compared to model simulations (broken lines) using experimental temperature data interpolated to 2x resolution. One model was run with surface vapor densities as measured (triangles) and several were run with assigned values of ρ (asterisks). Notice that the models agree below the depth where ice has accumulated, indicating gradient control by the saturation vapor pressure.

abundances compared to unshifted temperature data.

The maximum observed filling fraction is less than 100%, suggesting the possibility that the deposited ice is less dense than pure ice. This is consistent with micrograph images (see Figure 5.4) which show encapsulated bubbles and turbid ice. If the numerical model is modified such that the density of deposited ice is lower, the results can be made to match more closely with the experimental data. Figure 5.11 shows such results for four selected datasets and their attendant model runs using ice densities of 918 and 734 kg m^{-3}, the latter being equivalent to 80% maximum filling. Such a reduced density improves the model fit, but filling fractions up to 90% are observed in the longest experiment. In the simplest case it can be assumed that all deposited ice has the same density, which should be at least the maximum observed in any experiment, suggesting that

a density of 734 kg m^{-3} is too low. It is possible that the density of deposited ice varies depending on local geometric effects, temperature, and time of deposition. The density of the deposited ice is not measured directly and thus cannot constrain ice density as a function of time. Given this uncertainty and the observation of 90% filling (implied ice density $\sim$826 kg m^{-3}), another possibility is considered: non-linear constriction.

The model results presented thus far have used a linear relation between diffusivity and filling fraction, as used by *Mellon and Jakosky* (1993), to account for constriction. In this schema, the porosity at time t is

$$\phi(t) = \phi_0(1 - \frac{\sigma(t)}{\phi_0 \rho_{\text{ice}}}).$$
(5.4)

The ice-free diffusion coefficient $D_0 = D(\phi_0)$ is thereby modified by a factor of ϕ/ϕ_0. The constriction model of *Mellon and Jakosky* (1993) subsumes all variation in pore geometry into the value of the porosity, ϕ, and leaves the tortuosity term unaltered. This was justified due to a lack of experimental or theoretical data on the effects of constriction on tortuosity.

It is found, however, that agreement between the experimental data and the ice contents predicted by the models can be improved if the density is maintained at $\sim$918 kg m^{-3}, but the constriction factor is modified by an exponent, n:

$$D = D_0 \left(1 - \frac{\sigma}{\sigma_0}\right)^n.$$
(5.5)

The reduction of porosity (understood as the available area through which vapor can pass) due to deposited ice is linear in σ, hence the base model used here and that of *Mellon and Jakosky* (1993) assume $n = 1$. It can be seen in Figure 5.11 that models with $n = 1$ match the data well for filling fractions of $\sim$40% or less, but that they overpredict the amount of ice deposited for longer times with higher filling fractions. A model run for the 330 hour experiment, wherein filling fractions are >70%, which uses $n = 2$ and $\rho_{\text{ice}} = 918$ kg m^{-3} is plotted in Figure 5.11 as a red dashed curve and is seen to be in close agreement with the experimentally measured ice contents. The degree of agreement between this model and the experimental data is comparable to that between the data and the model with $n = 1$ and 80% ice density, but this scenario is not favored because observed densities reach at least 90%. Changes other than reduction of porosity, *e.g.,* the shortening of molecular hop distances as ice reduces the available volume, add additional constriction effects which cause a non-linear dependence of D on σ when filling fractions are large. In the model parameterization, these effects are captured in n, as described in Section 5.6.2.
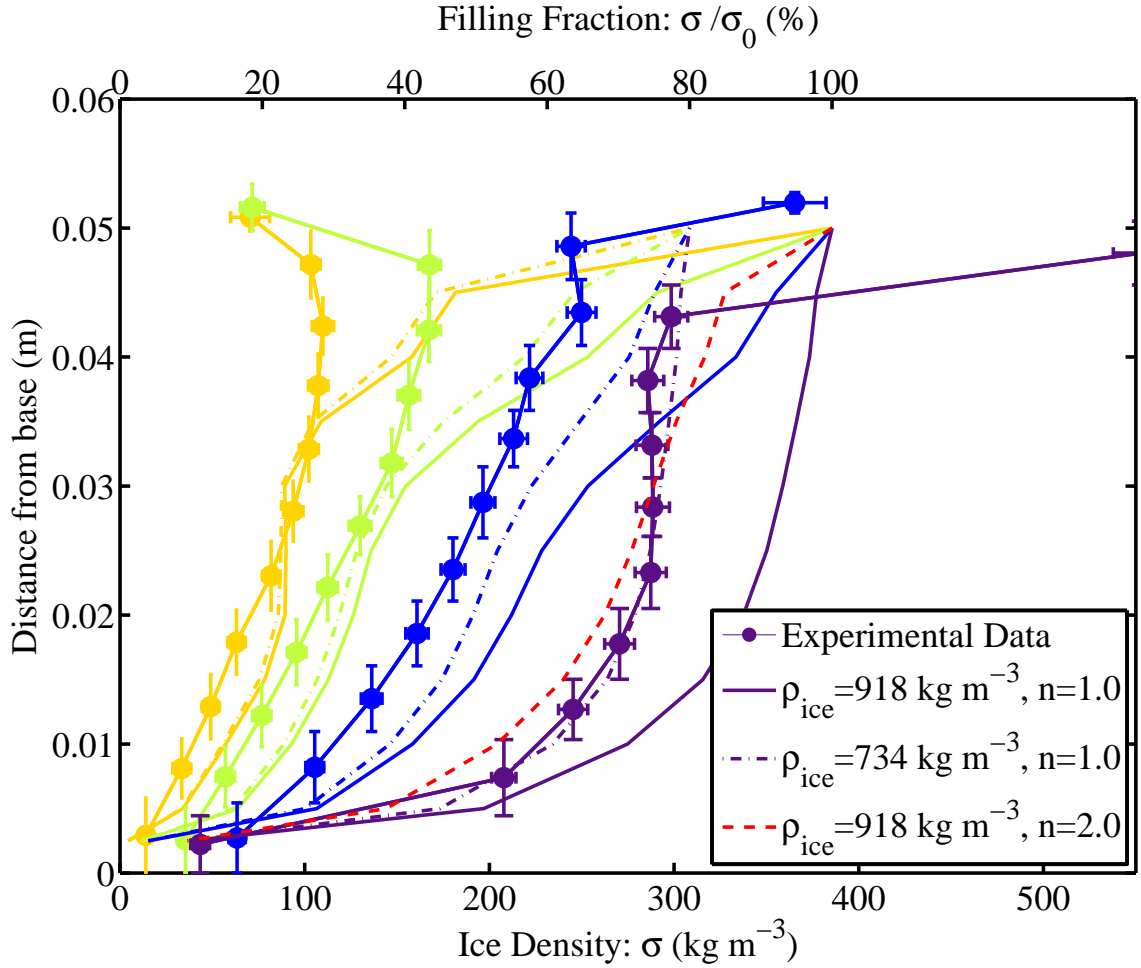
Figure 5.11: Experimental data and model outputs for 24, 48, 120, and 330 hour experiments. Experimental data are filled circles with error bars. Model results vary as the maximum density of deposited ice is changed, and the best agreement for the experiments with high filling fractions appears to be with $\rho_{ice} = 734$ kg m^{-3}, or 80% the density of pure ice. For times shorter than ~48 hours, models which assume diffusivity is linearly proportional to filling fraction agree with the experimental data. A single dashed line (in red) indicates the model output for the 330 hour experiment if 100% ice density is assumed, and diffusivity varies as the square of the filling fraction (*i.e.*, constriction exponent equals 2).

5.5.3 Time-varying diffusion coefficients

The diffusivity as a function of time can be extracted from the available experimental data by making the simplifying assumption that variations of D with depth are slow. The right hand side of Equation (2.26) may then be used to estimate the diffusion coefficient as a function of ice density. The relation used is:

$$\frac{\sigma(t+\delta t) - \sigma(t)}{\delta t} = D(t + \frac{\delta t}{2})\frac{1}{\delta t}\int_{t}^{t+\delta t} \frac{\partial^2 \rho_1}{\partial z^2} dt',$$

(5.6)

where δt indicates the time interval separating successive experiments. The accumulated quantity of ice in an interval, $\delta\sigma/\delta t$, divided by average values of the density divergence in the same interval
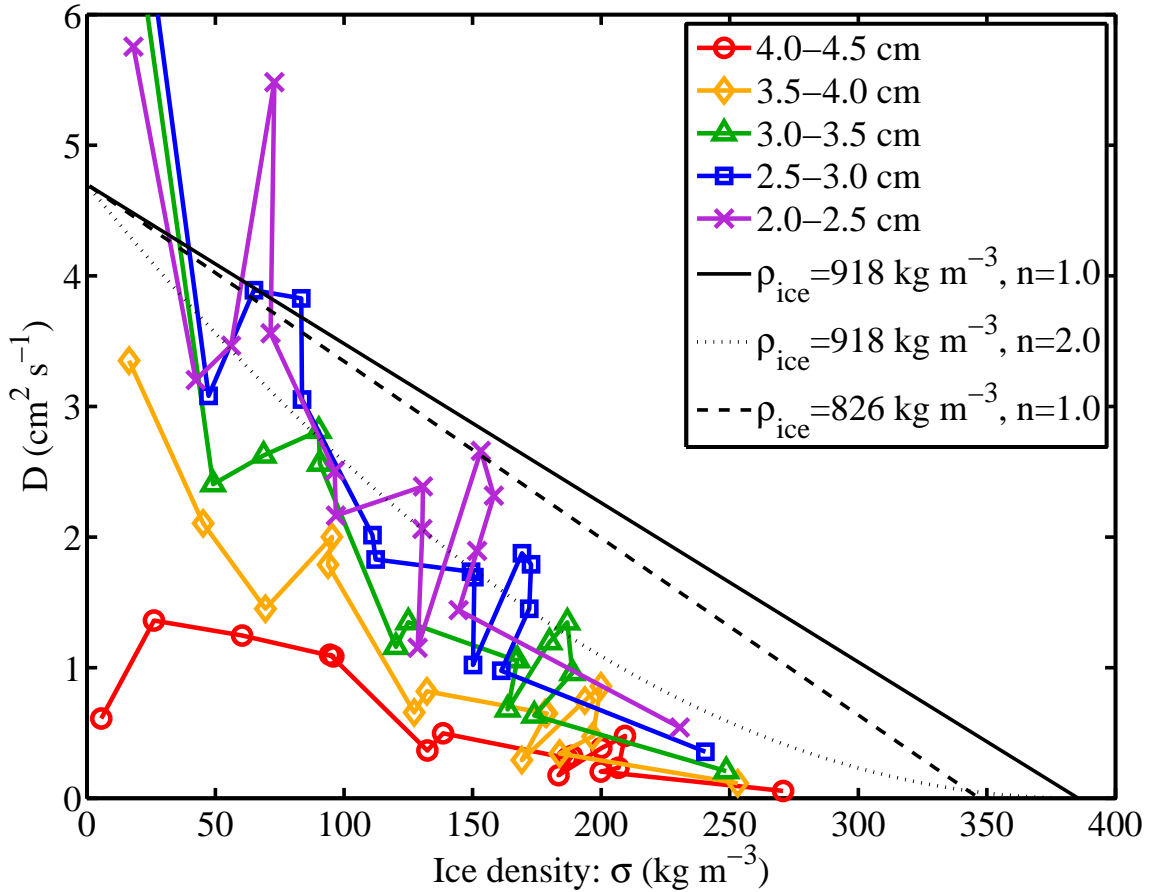
Figure 5.12: Plot of the diffusion coefficient evaluated using the technique described in Section 5.5.3 versus ice content for 5 deep levels in the sample column. Overplotted are expected variations in D with σ using $\rho_{\text{ice}} = 918$ kg m^{-3} for $n = 1$ (solid) and $n = 2$ (dotted). The trend in the diffusion coefficient exhibits a concave-upwards slope which is consistent with n greater than unity. If the density of deposited ice were 90% of pure ice density, and $n = 1$, the diffusion coefficient would follow the dashed line.

gives a proxy for D, which may be plotted versus the average ice content over δt at a particular depth. Figure 5.12 thus displays the change in diffusivity due to constriction in the deepest layers where the changes in ice content are easiest to observe.

Systematic differences among experiments result in a considerable scatter in Figure 5.12, but an overall trend to lower values of D can be discerned. The trends are consistent with the expected variation of D with σ for a constriction exponent greater than unity ($n = 1$ and 2 are plotted as solid and dotted lines, respectively). If n is constrained to be equal to unity, but the maximum ice density relative to free space is allowed to be less than 386 kg m^{-3}, then the linear trend (dashed line) would reach a smaller maximum value. But filling fractions of 90% imply a σ of at least 347 kg m^{-3}. The trend of D with σ using this lower density and $n = 1$ does not match the data as well as the data with a higher constriction exponent, suggesting that $D(\sigma)$ depends on σ and is non-linear for high

filling fractions.

The reduced deposition rate as a function of time exhibited by these data is consistent with the constriction phenomenon. The close agreement between the reduced rate of ice accumulation in models and experimental data improves confidence that the model employing non-linear adjustment of D with σ more closely captures the physics of the ice deposition process. Both effects of reduced ice density and non-linear constriction may be important in controlling the evolution of ice at high filling fractions obtained for long exposures to ice-growth conditions.

5.5.4 Long-duration behavior

The longest experiment was run for 530 hours of exposure to humid gas. The rate of change between the 330 and 530 hour experiments is small, indicating significant constriction in the shallow layers and concurrent reduction of ice deposition rates at greater depths. The numerical model has been run for 6000 hours of experiment time using a static, linear temperature profile of the same magnitude as used in the experiments. The other parameters are a constriction exponent of $n = 2$, an ice density of 918 kg m^{-3}, the total pressure of 600 Pa, and surface densities of 1.6 and 3.2 g m^{-3}.

Figure 5.13 plots the cumulative ice content as a function of time for the two model runs (broken lines), column-integrated ice contents for the experiments (filled symbols), and the local column ice density for the most ice-rich layer in each experiment, scaled by a factor of 10 (open symbols). The column integrated ice contents are computed over the depth of the ice-bearing sample. Both models are seen to converge asymptotically to the maximum theoretical ice content, σ_0/Z, with the difference being $< 5\%$ after $\sim$5000 hours. The experimental data agrees well with the model using the higher vapor density, particularly for times greater than 24 hours, corresponding to surface ice at 268 K, rather than the atmosphere, being the dominant vapor source.

The experimental data are consistent with the asymptotic approach of the ice content to total filling. Further experiments which achieve high filling fractions may improve understanding of the ice deposition process, potentially revealing important phenomena that only affect ice deposition when constriction effects are large.

5.6 Discussion

5.6.1 Theoretical uncertainties in vapor transport

The governing equation for the diffusive transport of water vapor (denoted by subscript 1) in CO_2 (denoted by subscript 2) is given by (*Landau and Lifshitz*, 1987)

$$J_1 = -\rho_0 \left[\mathcal{D}_{12} \frac{\partial}{\partial z} \frac{\rho_1}{\rho_0} + \frac{\mathcal{D}_T}{T} \frac{\partial T}{\partial z} \right], \tag{5.7}$$
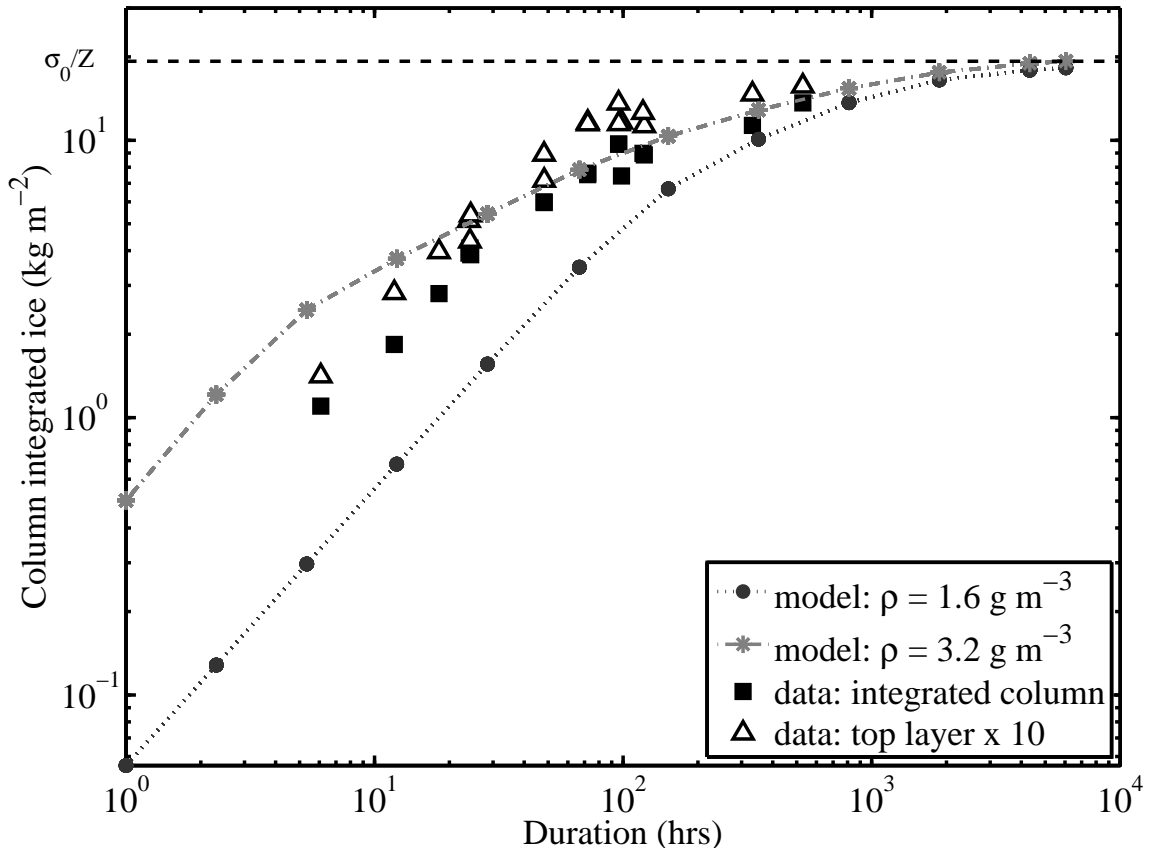
Figure 5.13: Column-integrated ice abundances for experiments and two long-duration models (parameters given in text). Solid symbols are integrated column densities, open symbols represent ice contents in the uppermost ice-bearing layer (*i.e.*, the most ice-rich layer) scaled by a factor of 10. Model runs with vapor densities of 3.2 g cm^{-3} match total ice abundances well after 24 hours, supporting the conclusion that the driving vapor density is that of the surface ice at 268 K. Maximum column density for ice in a 42% porosity medium would be $\sigma_0/Z = 19.3$ kg m^{-2}.

where J_1 is the diffusive mass flux of gas 1, ρ_0 is the total mass density, $\rho_0 = \rho_1 + \rho_2$, $\mathcal{D}_{12}$ the mutual diffusion coefficient in free-gas, $\mathcal{D}_T$ the coefficient for "thermodiffusion", and T the temperature. The contribution of barodiffusion to the vapor flux is neglected.

In *Hudson et al.* (2007) a review of the thermal diffusion effect is presented and is shown to be a negligible contributor to the vapor flux in the experiments described therein. Here, the issue is revisited for the high thermal gradients in the present experimental setup. The concentration-dependent thermal diffusion factor α_T is at most $\alpha_T \approx 0.8$ for H_2O–CO_2, using the conservative elastic sphere model (*Chapman and Cowling*, 1970). By definition $\mathcal{D}_T/\mathcal{D}_{12} = \alpha_T(n_1/n_0)(n_2/n_0)$, where n indicates number densities. At low concentration, $\mathcal{D}_T/\mathcal{D}_{12} \approx \alpha_T(\rho_1/\rho_0)(\mu_2/\mu_1)$, where μ_1 and μ_2 are the masses of H_2O and CO_2 molecules, respectively.

In equilibrium, the total H_2O flux vanishes, rendering the ratio of thermodiffusion flux to concentration-driven flux as an inappropriate measure. Instead, an estimate of the change in ice

table depth δz due to thermodiffusion in this laboratory setup is determined by

$$-\rho_0 \mathcal{D}_T \frac{1}{T} \frac{\partial T}{\partial z} = \frac{\partial J_1}{\partial z} \delta z. \tag{5.8}$$

The total diffusive flux J_1 is approximately, $-D_{12} \partial \rho_1 / \partial z$, and thus

$$\rho_1 \alpha_T \frac{\mu_2}{\mu_1} \frac{1}{T} \frac{\partial T}{\partial z} = \frac{\partial^2 \rho_1}{\partial z^2} \delta z. \tag{5.9}$$

From equation (5.1) and $H/(RT) \approx 23 \gg 1$, an approximate expression for $\partial^2 \rho_1 / \partial z^2$ is obtained and used in equation (5.9) to give,

$$\alpha_T \frac{\mu_2}{\mu_1} \approx \delta z \left(\frac{H}{RT} \right)^2 \frac{1}{T} \frac{\partial T}{\partial z}. \tag{5.10}$$

Hence, $\delta z \lesssim 8 \times 10^{-4}$ m, which is negligible compared with the relevant length scales.

The contribution of advection or bulk flow to the vapor transport is also small. The sample container has an impermeable bottom boundary, such that bulk motion can only be caused by the displacement of gas from the growing ice volume, surely negligible, and the contribution of the H_2O flux to the overall motion. The latter should be on the order of p_1/p_0; the maximum p_1 is reached at the ice table, where $p_{sv}(268 \text{ K}) = 397$ Pa, while $p_0 = 600$ Pa. Figure 5.1 demonstrates that rapid ice growth only occurs when the equilibrium vapor pressure of H_2O is not much smaller than the total pressure.

By eliminating the advective velocity from equations for the total flux of interdiffusing species, it is found that the inward flux is larger than what is obtained from diffusion alone by a factor of $\rho_0/(\rho_0 - \rho_1)$ (*Landau and Lifshitz*, 1987; *Hudson et al.*, 2007). This expression is not applicable for Knudsen diffusion, but qualitatively indicates that advection increases the flux in these experiments. For model runs greater than 48 hours, the excess ice relative to observations using a linear dependence of D on filling fraction, *i.e.*, $n = 1$, can therefore not be explained by an unaccounted advective contribution.

5.6.2 Constriction physics

In equation (5.5), an exponent, n, is introduced to modify the change in diffusion coefficient as a function of filling fraction. The changing geometry of the pore space during ice deposition results in a non-linear dependence of D on σ at high filling fractions. A cause of this phenomenon arises from reduced pore space volume, which results in a greater frequency of molecule–wall collisions for a given pressure. The effect of mean free path and molecular hop length on D can be seen in the following derivation.

The free-gas diffusivity may be approximately written as

$$D_{12} = \frac{1}{3}\bar{\nu}_1\lambda, \tag{5.11}$$

where $\bar{\nu}_1$ is the mean thermal speed of water molecules and λ is the mean free path. The Fickian diffusion coefficient in a porous medium may be written as

$$D_F = \frac{\phi}{\tau}D_{12}, \tag{5.12}$$

and the Knudsen diffusion coefficient may be written as

$$D_K = \frac{1}{3}\bar{\nu}_1 l\frac{\phi}{\tau}, \tag{5.13}$$

where l is a measure of characteristic hop length, and any prefactor is subsumed into the relation between l and pore size. This treatment is similar to the treatment of *Evans et al.* (1961), who derive a Knudsen diffusion expression which is also proportional to the obstruction factor, ϕ/τ. Since l is proportional to available pore size,

$$l = l_0\phi/\phi_0, \tag{5.14}$$

where l_0 is for the dry porous medium. Equations (5.2), (5.11), (5.12), (5.13), and (5.14) lead to

$$D = \frac{\phi}{\tau}\frac{\bar{\nu}_1}{3}\left(\frac{1}{\lambda} + \frac{1}{l}\right)^{-1}. \tag{5.15}$$

Hence, changes in D with ice content can be attributed to three contributions: porosity ϕ, tortuosity τ, and restriction in hop length l. If τ were constant with time, then D varies proportionally with ϕ when $\lambda \ll l$, and it varies as ϕ^2 for $\lambda \gg l$.

The diffusivity therefore changes from linear in σ to a stronger dependence as deposition progresses. At high filling fractions, the l term in equation (5.15) dominates over the λ term, the porosity term is small, and the tortuosity will become large as diffusive paths are closed off. Figure 5.11 shows that models with low filling fractions agree well with experimental data if the relationship between D and σ is linear, *i.e.,* the constriction exponent n equals 1, while models for long-term experiments with high filling fraction overpredict the ice abundance with $n = 1$. Equation (5.15) implies that the functional relationship between D and σ changes with σ, and a real system would not be described by a constant constriction exponent, as was employed in the model (Section 5.5.3). Further study of the constriction phenomenon may reveal the appropriate prefactors and dependencies to model this transition.

5.6.3   Initial ice deposition

The preferential deposition at grain contact points, as revealed by the micrographs in Figure 5.4, could first fill the smallest pore spaces and narrowest gaps between grains. Most of the flux in a medium of distributed pore sizes is carried in the largest pores (*Clifford and Hillel*, 1983, 1986), and this initial deposition should not greatly alter the effective diffusion coefficient. But this small amount of ice may still affect the availability of pathways to conduct vapor, changing the tortuosity of the medium.

Another consequence of ice deposition is a change in bulk thermal conductivity (*Paige*, 1992). The thermal conductivity of ice-free 500 μm glass beads used in these experiments is 0.18 W m^{-1} K^{-1} (*Ham and Benson*, 2004). This value is higher than the values of bulk thermal conductivity for particulate material used by *Mellon and Jakosky* (1995) (0.02 W m^{-1} K^{-1}). Ice, on the other hand, has a bulk thermal conductivity of $\sim$2.2 W m^{-1} K^{-1}. The addition of ice at grain contact points greatly increases the conductivity of the sample through increased area of heat conduction and the high thermal connectivity of the added material. The effect of included ice on the bulk conductivity of an ice-bearing soil was represented in *Mellon et al.* (1997) by the action of two parallel conductors where the contribution of ice in the intergrain space was proportional to the square root of the filling fraction, $(\sigma/\sigma_0)^{1/2}$ in the notation used here. This model exhibits a rapid increase in thermal conductivity for small filling fractions. The effect of the earliest deposited ice is significant with respect to its effect on the thermal properties of the regolith.

5.6.4   Ice growth physics and phenomenology

An initially dry soil subjected instantaneously to a moist atmosphere will experience a rise in vapor density at all depths until saturation is reached, or an unsaturated gradient is established between the surface and the saturation depth (shown schematically in Figure 5.14 as point B). Initially, point B is the top of the ice table, and the density gradient between this depth and the atmosphere must be linear if no ice is deposited in this region.

The nonlinearity of the vapor density gradient (exponential temperature dependence) results in the greatest quantity of ice being deposited at the top of the transient ice table. The gradients of the vapor density in the ice-bearing and ice-free regions are equal at the interface, and initially the fluxes are as well. But constriction reduces the diffusion coefficient and flux through an ice-bearing layer while leaving the vapor density gradient unaffected. Conservation of mass then requires that the flux in the ice-free region also be reduced. Since in this region the flux depends only on the vapor density at the surface and the depth to the ice table, the interface must move upwards, from point B toward point C.

As the interface becomes shallower, the gradient of vapor density through the ice-free region is
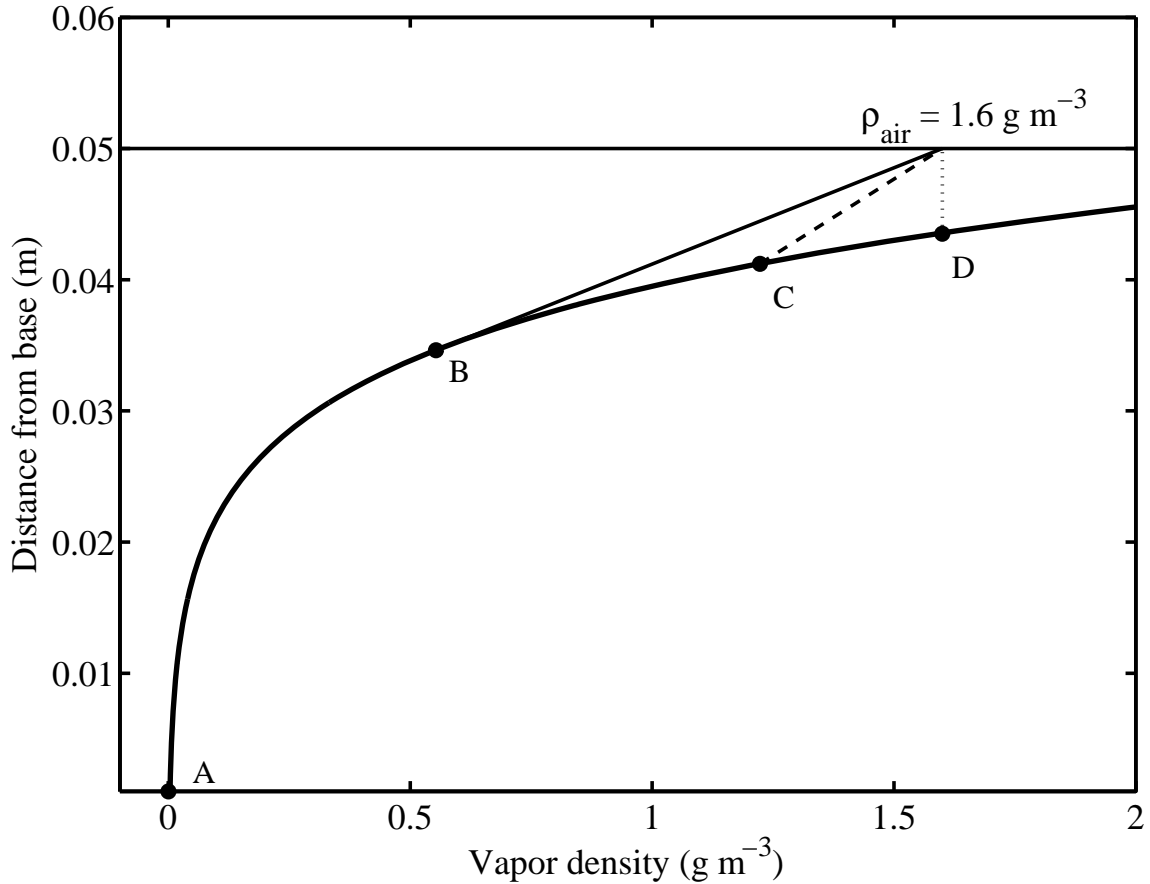
Figure 5.14: The steady-state vapor density for a sample with a 13 K cm^{-1} temperature gradient. For levels where ice is present, the vapor density is set by the saturation vapor pressure of ice (thick curved line). For levels with no ice present, the gradient is linear (or approximately so) between the saturation line of the uppermost ice and the atmospheric vapor density, which is here set at 1.6 g m^{-3}.

diminished, thus ultimately reducing the flux to the ice table and the rate of ice deposition. Since small changes in depth correspond to large changes in vapor density gradients in steep regions of the saturation curve, the rate of ice table migration slows. The difference in rates of ice growth between deep and shallow depths decreases with time, and the ice-content profile becomes progressively more uniform. This occurs despite the higher gradients at shallow depths because greater ice contents restrict vapor flux.

At all times, the ice beneath the ice table interface continues to evolve down-gradient. Water vapor surrounded above and below by ice feels only the local vapor gradient due to temperature; it is independent of the atmospheric density. If the atmospheric water content were to drop sharply, the ice table would begin to recede from the top down. Existing subsurface ice would continue to migrate deeper until all ice above it was removed and it was able to feel the effect of the vapor density gradient (now reversed in sign) in the ice-free region above.

If the atmospheric vapor density remains high, the ice table will evolve toward its equilibrium at point D. At equilibrium, the gradient in the ice-free region and the inward flux must be zero. But since ice beneath the ice table is continuously redistributing down gradient, there must remain a positive net flux into the subsurface. Thus the ice table interface must be beneath the equilibrium depth so long as the porous medium is unsaturated down to some zero-flux boundary. Substantial constriction permits only small fluxes, allowing the ice table to be close to the equilibrium position when filling fractions are high. If the climate on Mars has been stable enough to permit substantial filling, differences between equilibrium predictions of ice table depth (*e.g., Mellon et al.* (2004); *Schorghofer and Aharonson* (2005)) and observed depths (within the accuracy achievable by spacecraft such as Mars Odyssey and the Phoenix Lander) are unlikely to be large.

Where the conditions have been favorable to ice growth for long times, the filling fraction in the layers of the regolith immediately beneath the ice table may approach saturation. But since there is a non-zero flux to some depth, the shallow ice must remain porous to accommodate this transport. In situations with very high filling fractions, where pore spaces are no longer continuous, downward flux may persist through the mechanism of counterdiffusion of water molecules and lattice defects or vacancies.

In a stable environment, complete choking of the regolith column, meaning zero flux to deeper depths, will not occur until all available pore spaces are filled. The volume which is available for filling will depend on the depth of the zero-flux boundary. This may either be some layer in the regolith with zero diffusivity or the inflection depth of the mean annual vapor density gradient, as determined by the conductivity of the regolith, the local temperature environment, and the geothermal gradient.

5.6.5   Voluminous pore ice on Mars

Two mechanisms by which significant volumes of ice can be emplaced in the shallow subsurface of Mars are 1) precipitation and subsequent burial and 2) inward diffusion of atmospherically derived vapor. The former process requires climate conditions significantly different from those currently observed, while the latter may have operated frequently in the past in addition to being active today.

Most unconsolidated sandy terrestrial soils have porosities between 30–50% (*Taylor*, 1977), though finer particulates can give rise to porosities up to 60% (*Baver*, 1940). Even including constriction, near-complete filling of such void fractions can occur at present-day conditions in $\sim 10^5$ years, resulting in ice contents approximately equal to the ice-free porosities. Climate changes which destabilize subsurface ice may reset shallow ice contents to zero periodically, preventing the depths accessible by remote sensing from attaining complete filling.

The Gamma Ray Spectrometer on board Mars Odyssey measured mid- to high-latitude hydrogen abundances equivalent to up to 70% ice by volume (*Prettyman et al.*, 2004). Ice contents of this magnitude would require precipitation and burial, the subsurface growth of pure ice lenses, or

unusually high initial porosities which may be filled by diffusion. The presence of polygonal terrain on Mars shows that a mechanism capable of moving soil grains has been active in these regions. Liquid water films, an important component of ice-wedge formation on Earth (*Konrad and Morgenstern*, 1980; *Konrad and Duquennoi*, 1993; *Dash et al.*, 1995; *Wettlaufer*, 1999), are not favored on Mars at present. Thermal contraction cracking (*Mellon et al.*, 1997) may play a dominant role in the dynamics of presently forming polygons (*Mellon et al.*, 1997). No evidence of heaving, lensing, or grain-segregation is observed in this static-environment experimental setup, but this is not surprising given the absence of a thermal wave oscillation. It should also be noted that microscopic effects of grain movement accumulate over long times, and cracking due to the stress of thermal contraction require distances on the order of a polygon diameter (10s to 100s of meters) (*Mangold*, 2005), much greater than the times and length-scales characteristic of these experiments.

Fisher (2005) suggests that thermal cracking of solid (perhaps interstitial) ice due to seasonal temperature variations may serve to keep deep regolith more open to vapor transport despite constrictive flux reduction in shallow layers. Cracks could penetrate into an otherwise ice-saturated soil, opening up further volume for subsurface deposition. Ice wedges on Earth form through the trapping of seasonal meltwater in the thermal cracks. The absence of a liquid phase on present-day Mars would tend to favor sand-wedge formation. But vapor propagation through the space opened by the crack would be enhanced over porous medium diffusion, and material at the base of the crack is shielded from direct insolation and will therefore remain cold relative to the surface. Ice wedges on Mars may therefore arise from vapor diffusion processes. If the combined volume of the vertically penetrating ice veins arising from such cracks is large, they could contribute to high observed ice contents.

5.6.6 Phoenix Mars lander

The Phoenix Mars Lander will land in the north polar region of Mars where equilibrium models and neutron spectrometer data from the Mars Odyssey spacecraft predict the presence of subsurface ice within centimeters of the surface (*Boynton et al.*, 2006; *Arvidson et al.*, 2008; *Mellon et al.*, 2008). The lander is equipped with a robotic arm which will be able to trench on the order of half a meter into relatively unconsolidated surface regolith; excavation down to the ice table is one of the primary mission goals (*Arvidson et al.*, 2008). In doing so, Phoenix will be able to provide a number of ground truths regarding the behavior of subsurface ice on Mars.

The robotic arm has limited mechanical strength and leverage and may be unable to penetrate deeply through soil with a high ice content, or through pure ice if it is not highly porous. Despite this limitation, the Phoenix arm may be able to sense an abrupt change in mechanical strength of the regolith which would indicate a sharp ice table as predicted theoretically and as has been seen in these experiments. Using the rasping tool at the scoop, Phoenix will attempt to remove some

surface layers of the shallow ice table. Photographic analysis of these raspings and the divots made in the ice table, as well as planned delivery of icy regolith to various on-deck instruments, may constrain the soil-to-ice mixing ratio. This could illuminate whether this ice was diffusively derived, as would be suggested by a low to moderate ice-to-soil ratio, or was emplaced by precipitation and subsequent burial, consistent with a high ratio.

If the ice-bearing regolith has a sufficiently low mechanical strength that it may be penetrated by the robotic arm, it may be possible to create a cross-section of the regolith column revealing the ice table interface. The morphology of the ice table could be correlated with the original surface albedo and rock distribution. Though it is not equipped with a brush to remove unconsolidated debris, a number of such profiles, as from a widening trench, may allow a coarse three-dimensional map of the ice table to be developed.

Low mechanical strength of the ice-bearing soil layers would be indicative of filling fractions less than 100%. Though not equipped with means of directly determining water content, Phoenix instruments such as the Thermal and Evolved Gas Analyzer (TEGA) and the Thermal and Electrical Conductivity Probe (TECP) may be able to constrain this quantity. Incomplete filling would be indicative of a non-equilibrium state which is continuing to evolve over time, constraining the history of the temperature and atmospheric water content at the landing site. Combined data sets from measurements of soil thermal conductivity and optical microscope images of the regolith particles will help constrain other soil properties, such as diffusivity, which are necessary inputs to understanding the history of subsurface ice.

5.7 Summary

A Mars environment chamber has been used to demonstrate the diffusive filling of regolith pore spaces from atmospherically derived water vapor in the absence of a bulk liquid phase. This allows the first examination of bulk ice deposition via vapor diffusion at low pressures in the laboratory. This process is studied at three scales.

At the scale of individual soil grains, optical micrographs have revealed preferential deposition at grain contact points, forming ice necks in close association with regolith particles which should significantly affect the thermal conductivity. Much of the deposited ice is turbid, suggesting the presence of grain boundaries, vacancies, or trapped gases within the ice which would reduce its bulk density. Bubbles on the order of 10–20 μm across have been observed trapped in the ice, suggesting that ice on Mars deposited through vapor diffusion may be a candidate for the extraction of trapped atmospheric gases.

At the scale of the ice table, measurements of the transition depth have revealed the sharpness and shape of the contact. The transition between well-cemented and completely unconsolidated

grains is on the order of a single grain diameter ($\sim$500 μm). The morphology of the interface is sensitive to the local temperature field and is affected by surface irregularities such as heat pipes (*e.g.*, a warm probe head or a rock) and albedo variations (*e.g.*, coated disks or dust patches), and the magnitude of these perturbations decays with depth. The ice table follows temperature isotherms, which parallel the surface unless perturbations arising from, for example, albedo differences, deflect the temperature field.

Finally, at the deeper scale of the "cryosphere", *i.e.,* the ice beneath the dry interface, the quantity and distribution of ice as a function of depth and time has been revealed through gravimetric water content analysis. A series of experiments and numerical models of differing atmospheric vapor densities illustrate the sensitivity of ice table growth rate to the humidity of the atmosphere, and the insensitivity of ice at depths beneath the ice table to this same quantity. The evolution of the cryospheric ice beneath the ice table depends only on the local temperature gradient.

The deposition of ice significantly reduces subsequent deposition rates via a process of pore-space constriction. Numerical models of the experimental conditions which incorporate constriction capture the major effects of that process with a parameterized modification of the diffusion coefficient proportional to filling fraction. Although some observed differences between experiments and models may involve a lower density of deposited ice, observations of 90% filling after 530 hours show that the minimum density is at least this much. At intermediate filling, a stronger obstruction than linear in filling fraction is observed. The simultaneous reduction of available porosity and of molecular hop length (*i.e.,* the increasing frequency of collisions with pore walls) as ice is deposited results in an expected dependence of D proportional to the square of the filling fraction, consistent with measurements when the filling fracton is high. The tortuosity may also change at moderate to high filling fractions, further increasing the sensitivity of D to σ. Further investigation is needed to describe the constriction at high filling fraction.

The numerical model is used to examine long-term growth effects under simulated temperature and humidity conditions. The effect of constriction asymptotically diminishes the vapor flux beneath the ice table and similarly retards the ice deposition rate.

The complete filling of the regolith with atmospheric vapor on obliquity-scale times will be inhibited by reduced rates of ice deposition due to constriction, but complete choking will not occur unless the pore volume is completely saturated with ice. Lack of complete filling in a regolith column implies a nonequilibrium condition such that the quantity and distribution of subsurface ice is continually evolving. These studies will inform observations of subsurface ice by Phoenix and subsequent spacecraft addressing similar regions.